Triple Modal Coherent Nonlinear Imaging With Vibrational Contrast

Adam M. Hanninen, Richard C. Prince, and Eric O. Potma

(Invited Paper)

Abstract—By combining spectroscopic contrast with imaging speed, coherent Raman scattering (CRS) microscopy techniques have reiterated the usefulness of vibrational microscopy. In the nonlinear optical (NLO) microscope, CRS is often combined with other nonlinear optical signals, such as two-photon excited fluorescence or second-harmonic generation, providing images with multimodal contrast. However, it is also possible to expand the vibrational capabilities of the NLO microscope, namely through incorporation of other vibrationally selective nonlinear optical signals beyond CRS. Recently, it has been shown that vibrationally resonant sum-frequency generation (SFG) microscopy can be integrated into the imaging platform as well, offering additional vibrational spectroscopic probing capabilities. In this contribution, we highlight the concept of triple-modal vibrational microscopy, which combines CRS, SFG, and third-order sum-frequency generation on a single laser-scanning microscope. These three vibrationally sensitive NLO imaging techniques provide complementary information about the sample, allowing for more detailed molecular spectroscopic studies of biological specimens. We review the principles of the three light-matter interactions that underlie the techniques and discuss some of the imaging properties of the triple-modal vibrational microscope. We provide several imaging examples and conclude with discussing some of the outstanding challenges.

Index Terms—Nonlinear optics, microscopy.

I. INTRODUCTION

IN COHERENT nonlinear optical spectroscopy, molecules are driven in unison with laser beams to induce a coherent radiative response. The coherent excitation of an ensemble of molecules can reveal important information about the dynamics of relevant molecular states, information that is often difficult to obtain from linear spectroscopy measurements [1]. In addition, the coherent driving mechanism gives rise to a signal that benefits from the aligned phases of the waves radiated from the sample. The resulting mutual constructive interference between the waves produces a signal that can be of appreciable magnitude in a phase-matched direction. This latter property of signal coherence can be useful for amplifying otherwise weak optical effects. Coherent Raman scattering (CRS) is a prime example of a nonlinear optical technique that takes advantage of the coherent amplification of the optical response, yielding signals that can be orders of magnitude stronger than linear Raman signals.

The stronger signals afforded by the coherence among the driven molecules have enabled CRS measurements of very small sample volumes at rapid signal acquisition speeds. CRS microscopy makes use of this capability, offering vibrational Raman signals from microscopic volumes with pixel dwell times of microseconds or less [2]–[4]. Coherent anti-Stokes Raman scattering (CARS) and stimulated Raman scattering (SRS) microscopy are both successful implementations of CRS, enabling real time imaging applications with vibrational spectroscopic contrast [5], [6], despite the intrinsic weakness of the Raman scattering effect. Laser-scanning CRS microscopy has matured into a trusted imaging tool with applications in cell and tissue biological research [7], [8], as well as pharmaceutical research [9]–[11], food science [12], [13] and material analysis [14]–[16].

The success of CRS microscopy has opened the door to adopting other forms of coherent vibrational spectroscopy as imaging contrast mechanisms in laser-scanning microscopy. In this regard, it would be particularly useful to have access to spectroscopic signatures that are complementary to those provided by CRS. Since CRS methods probe Raman active molecular modes, additional spectroscopic information is obtained through methods that probe vibrational modes with strong infrared (IR)-activity. Vibrationally sensitive sum-frequency generation (SFG) is a coherent spectroscopic technique that uses infrared radiation to drive a vibrational mode, followed by a Raman interaction to generate a signal in the visible or near-IR range [17], [18]. The SFG light-matter interaction has been successfully used as a contrast mechanism in microscopy [19]–[27], and has recently been integrated into a laser-scanning microscope [28]. Like second-harmonic generation (SHG) microscopy [29], laser-scanning SFG microscopy is sensitive to non-centrosymmetric structures such

as fibrillar collagen, which display a non-vanishing second-order susceptibility $\chi^{(2)}$. With SFG microscopy it is possible to visualize such structures with spectroscopic vibrational contrast, thus enabling a deeper analysis of molecular structure than what is possible with nonresonant SHG microscopy. Bulk-sensitive SFG microscopy has been used to study collagen-rich tissues [30], [31], cellulose fibers [28], [32] and biomolecular micro-crystals [33].

Adding a SFG module to the laser-scanning CRS microscope enables a more complete vibrational spectroscopic analysis of the sample. Advances in coherent light sources and microscope optics have made it possible to perform multi-modal CRS and SFG imaging studies [28]. However, although SFG adds complementary contrast to CRS images, it does not constitute a direct IR-active analogue of the Raman-based contrast of the CRS microscope. First, since SFG signals originate from non-centrosymmetric structures, SFG microscopy is only sensitive to particular molecular assemblies and materials. On the other hand, CRS microscopy probes the bulk-allowed $\chi^{(3)}$ properties of the specimen. This implies that CRS contrast is not restricted by the condition of non-centrosymmetry, thus opening up its application to a wider range of samples. Second, the vibrational modes probed in the SFG interaction must exhibit both Raman and IR-activity. Consequently, SFG is sensitive to a only sub-set of the Raman-active modes, thereby suppressing vibrational modes that are predominantly IR-active (with little to no Raman activity).

An alternative excitation scheme that involves an IR excitation followed by a two-photon up-conversion would fill the remaining void left by CRS and SFG vibrational microscopy. This third-order sum-frequency (TSFG) process, which relies on the $\chi^{(3)}$ response of the material, is bulk-allowed and sensitive to IR-active modes. Versions of the TSFG interaction have been used in electronically resonant and non-resonant fashion in microscopy [34], [35], bearing a close resemblance to third-harmonic generation (THG) imaging [36]–[38]. Vibrationally sensitive forms of TSFG have been used in (bulk) spectroscopy studies, using two-photon IR excitations to induce vibrational transitions [39], [40]. So far, TSFG has not yet been used to generate vibrationally sensitive images in a laser-scanning microscope.

In this contribution, we discuss the possibility to perform imaging studies with vibrational contrast provided by CARS, SFG and TSFG. All three techniques are sensitive to vibrational molecular motions and produce coherent optical signals. The combination of these nonlinear optical methods on a single imaging platform permits a complete vibrational spectroscopic assessment of the sample at high spatial resolution. We provide a brief overview of the capabilities of these nonlinear optical processes and describe how they can be integrated into a laser-scanning microscope. In particular, we report the first TSFG images with vibrational contrast. In addition, we point out some interesting imaging properties of the different modalities and present examples of multi-modal vibrational imaging of micro-structured samples. Finally, we discuss the prospects and challenges of triple-modal vibrational nonlinear microscopy in the context of biomedical imaging.
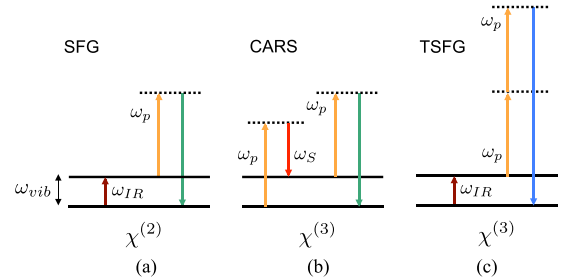

Fig. 1. Jablonski diagrams of the (a) SFG, (b) CARS and (c) TSFG processes.

TABLE I
PROPERTIES OF SFG, CARS AND TSFG IMAGING METHODS

Properties	SFG	CARS	TSFG
Mode selectivity	IR + Raman active	Raman-active	IR-active
Susceptibility	$\chi^{(2)}$	$\chi^{(3)}$	$\chi^{(3)}$
Sample symmetry	non-centrosymmetric	all	all
Power dependence	$I_{IR}I_p$	$I_p^2 I_S$	$I_{IR}I_p^2$
Lineshape	dispersive	dispersive	dispersive
Conc. dependence	c^2	c^2	c^2
Gouy $\Delta\Phi_g$	$< \pi$	≈ 0	$< 2\pi$
Lateral resolution	sub-μm	sub-μm	sub-μm

II. COHERENT VIBRATIONAL MICROSCOPY

A. Probing Vibrational Coherences

The SFG, CARS and TSFG techniques derive their vibrational sensitivity from the induced vibrational coherence in the sample. In SFG and TSFG, this coherence between the ground-state and the vibrationally excited state of the molecule is established with an IR pulse of frequency ω_{IR}, tuned to the frequency difference ω_ν between the molecular states. In CARS, the vibrational coherence is driven by two light fields at frequencies ω_p (pump) and ω_S (Stokes) through a Raman interaction, such that $\omega_p - \omega_S = \omega_\nu$. To probe the vibrational coherence of the sample, both SFG and CARS use an anti-Stokes Raman interaction to translate the magnitude of the coherence at ω_ν into signal field amplitude. Hence, if the ω_p field is used as the probe, then both SFG and CARS generate signals at $\omega_p + \omega_\nu$, which typically corresponds to a frequency in the visible or near-IR (NIR) range of the spectrum. On the other hand, the TSFG probing interaction is based on an anti-Stokes hyper-Raman process, producing a signal at $2\omega_p + \omega_\nu$. Fig. 1 shows the Jablonski energy diagrams for the three nonlinear processes. Table I summarizes several key properties of the SFG, CARS and TSFG techniques.

B. Selection Rules

The CARS process involves two sequential Raman interactions. Therefore, it probes vibrational modes that are Raman-active, i.e. that display a change in the (electronic) polarizability upon a displacement of the nuclei. Vibrational modes that are highly symmetric are usually highly Raman-active.

The SFG process includes a direct dipole-allowed transition followed by an anti-Stokes Raman interaction. This excitation scheme is sensitive to modes that are both IR and Raman-active [17], [41]. In practice, many vibrational modes

of biomolecules exhibit the required combined IR and Raman activity.

The TSFG process relies on a dipole-allowed vibrational transition, which imposes that the mode be IR-active. Modes that produce a change in the electric dipole moment as a function of the nuclear displacement are IR-active. The anti-Stokes hyper-Raman probing interaction of the TSFG process is sensitive to IR-active modes as well [42], [43]. Although hyper-Raman interactions also probe modes that are non-IR-active, the latter modes are not registered in the overall TSFG nonlinear process, which is thus only sensitive to IR-active modes. Hence, the spectral properties of the TSFG technique are expected to be closely related to the sample's infrared absorption spectrum.

C. Nonlinear Susceptibilities

The magnitude and frequency-dependence of the nonlinear optical signals can be estimated from expressions for the material's nonlinear optical susceptibility $\chi^{(n)}$, as obtained through perturbation theory in the semi-classical framework [1]. Here n is the order of the light-matter interaction, which is $n = 2$ for SFG and $n = 3$ for CARS and TSFG. The nonlinear susceptibilities are tensors of rank 3 ($n = 2$) and 4 ($n = 3$), which relate the vectorial components of the incident fields to the vectorial components of the induced polarization in the material. However, to simplify the discussion here, we will ignore the tensor character of the nonlinear susceptibility and instead study some of its properties in scalar form. In this context, the nonlinear optical susceptibilities probed in each of the three vibrationally sensitive methods can be summarized as:

$$\chi^{(2)}_{SFG}(\omega_{IR}) = \chi^{(2)}_{nr,SFG} + \chi^{(2)}_{r,SFG}(\omega_{IR}) \tag{1}$$

$$\chi^{(3)}_{CARS}(\omega_p - \omega_S) = \chi^{(3)}_{nr,CARS} + \chi^{(3)}_{r,CARS}(\omega_p - \omega_S) \tag{2}$$

$$\chi^{(3)}_{TSFG}(\omega_{IR}) = \chi^{(3)}_{nr,TSFG} + \chi^{(3)}_{r,TSFG}(\omega_{IR}) \tag{3}$$

All the nonlinear susceptibilities above include a vibrationally non-resonant term $\chi^{(n)}_{nr}$ and vibrationally resonant $\chi^{(n)}_r$ term. The nonresonant terms result from electron motions in the molecule without direct involvement of the nuclear modes. The nonresonant contributions introduce a background, which, in some cases, can be strong and overwhelm the vibrational contributions to the signal. Note that the nonresonant contributions for the different techniques correspond to different electron motions and thus have different values, i.e. $\chi^{(3)}_{nr,CARS}$ and $\chi^{(3)}_{nr,TSFG}$ are not the same. The vibrationally resonant terms are explicitly frequency dependent and can be written as:

$$\chi^{(2)}_{r,SFG}(\omega_{IR}) = \sum_\nu \frac{a_\nu}{\omega_\nu - \omega_{IR} - i\gamma_\nu} \tag{4}$$

$$\chi^{(3)}_{r,CARS}(\omega_p - \omega_S) = \sum_\nu \frac{b_\nu}{\omega_\nu - (\omega_p - \omega_S) - i\gamma_\nu} \tag{5}$$

$$\chi^{(3)}_{r,TSFG}(\omega_{IR}) = \sum_\nu \frac{c_\nu}{\omega_\nu - \omega_{IR} - i\gamma_\nu} \tag{6}$$

The summation is over the molecular states ν and the dephasing parameter γ_ν is a measure of the homogeneous linewidth of

the transition from the ground state to state ν. The parameters a_ν, b_ν and c_ν are proportional to the transition dipole moments involved in each of the nonlinear interactions. It can be seen that $\chi^{(2)}_{SFG}$ and $\chi^{(3)}_{TSFG}$ are both resonant when ω_{IR} approaches a vibrational frequency ω_ν. In CARS, the nonlinear susceptibility is enhanced when $\omega_p - \omega_S$ approaches ω_ν.

In all cases, the signal is generated at a frequency different from the frequency of the incident fields. The amplitude of the signal field is proportional to the nonlinear susceptibility. The far-field photo-detector is sensitive to the square of the signal field, which implies that the detected signal $S(\omega)$ is proportional to $\left|\chi^{(n)}\right|^2$. This is the so-called homodyne detection mode, as the signal field is not mixed with another reference field but detected as a complex product with itself. The modulus square of the nonlinear susceptibility introduces mixing terms between the resonant and nonresonant contributions:

$$S(\omega) \propto \left|\chi^{(n)}_{nr}\right|^2 + \left|\chi^{(n)}_r(\omega)\right|^2 + 2\chi^{(n)}_{nr}\text{Re}\left\{\chi^{(n)}_r(\omega)\right\} \tag{7}$$

The last term on the right hand side of Eq. (7) gives rise to a dispersive lineshape. The stronger the nonresonant contribution relative to the vibrational contribution, the more dispersive the band profiles. Because in typical CARS applications the nonresonant component can be substantial, the lineshapes exhibit a significant dispersive character [44]. Although $\chi^{(2)}_{nr}$ is often smaller in SFG applications, homodyne-detected SFG band profiles are nonetheless inherently dispersive. Based on similar arguments, it is expected that the spectrally-resolved TSFG signal also displays dispersive lineshapes.

In the homodyne detection scheme, all three nonlinear processes shown in Fig. 1 are parametric, i.e. the initial and final states of the molecule are the same, implying that no effective energy transfer has taken place between the light fields and the molecule [45], [46]. The molecular resonances thus act as facilitators in transferring energy between the light fields, without explicitly absorbing energy. This does not mean that the material remains cold while illuminated with the incident pulses, as there are other processes such as linear heating at ω_{IR} or Raman heating at $\omega_p - \omega_S$ (through SRS) that occur simultaneously.

D. Phase Matching

As in all forms of coherent spectroscopy, efficient transfer of energy from the incident fields to the signal field can only take place under proper phase matching conditions. The polarization induced by the incident fields must sustain a spatial phase in the interaction volume that mimics the phase of a propagating signal field. If the phase difference $\Delta\Phi$ between the propagating field and the induced polarization is larger than π, energy cannot be efficiently transferred to the signal field. The phase difference is found as $\Delta k \cdot L$, where Δk is the difference in the wavevector projections of the interacting fields in a chosen propagation direction, and L is the distance over which the fields interact. In SFG, CARS and TSFG, the wavevector mismatch Δk is not zero. However, if L is sufficiently short, the product $\Delta k \cdot L$ can still be smaller than π and thus phase-matching can be achieved [47].

In nonlinear coherent microscopy, the incident fields are commonly focused in the sample in a collinear fashion with the aid of a high numerical aperture (NA) lens. In this scenario, the fields only interact over a distance of a few μm or less in the main propagation direction. When the signal is collected in the forward propagating direction, $\Delta k \cdot L$ is smaller than π for all three nonlinear techniques discussed here, including TSFG. Consequently, the signal is not limited by phase shifts due to the wavelength dependent wavevector mismatch. However, another source of phase differences between the interacting fields, namely the Gouy phase shift, can affect the magnitude and propagation direction of the signal. The Gouy phase shift is an additional $\phi_i = \pi$ phase shift that a field E_i accumulates when propagating through a focal waist. In CARS, the Gouy related phase difference is $\Delta\Phi_g = 2\phi_p - \phi_S - \phi_{sig}$, where ϕ_{sig} is the Gouy phase shift of the signal field. Because the π phase shift is accumulated within approximately 1 μm of propagation lengths for all beams, the effective Gouy phase difference is $\Delta\Phi_g \approx 2\pi - \pi - \pi \approx 0$. The CARS signal is thus not significantly affected by the Gouy phase shift [47].

In SFG, on the other hand, $\Delta\Phi_g = \phi_{IR} + \phi_p - \phi_{sig}$. Using the same reasoning as above, we obtain $\Delta\Phi_g \approx \pi$, which would be significant enough to affect the energy transfer to the signal field, especially along the on-axis propagation direction. Indeed, the Gouy phase mismatch of about π is the reason for the off-axis radiation profiles that are familiar in SHG microscopy [48], [49]. In SFG, however, the focal depth of the ω_{IR} field is significantly larger than that of the other fields, which means that the interaction between the fields does not take place over the entire distance over which the ϕ_{IR} phase shift evolves. Effectively, $\Delta\Phi_g < \pi$ and the radiation profile in collinear SFG microscopy is expected to be less affected by the Gouy phase shift than is typical in SHG microscopy.

A similar comparison is relevant for TSFG microscopy, which is closely related to THG imaging. It is well known that the Gouy phase mismatch in THG microscopy amounts to about 2π, which is substantial and effectively suppresses the forward propagating signal from bulk materials [48], [50]. This large phase mismatch is the reason for the sensitivity of THG to interfaces and sub-wavelength interfacial structures. In TSFG, which substitutes one of the fields with a field of longer wavelength, it can be predicted that $\Delta\Phi_g < 2\pi$. However, the Gouy-related phase mismatch is larger than π, so significant distortion of the radiation profile can be expected which may suppress the signal from bulk materials.

The effective phase shifts are ultimately determined by the details of the spatial phase of the focal fields. These parameters are primarily determined by the wavelength of light and the characteristics of the focusing lens. For the reflective objective used in the studies described herein, the axial extent of the focal volume is significantly larger than what is common for the depth of focus achieved with refractive objectives. We may therefore expect somewhat different phase-matching conditions relative to the situation with refractive high numerical optics. We will discuss this point in more detail in Section IV-C.

III. NONLINEAR OPTICAL MICROSCOPE FOR MULTI-MODAL VIBRATIONAL IMAGING

A. Light Source

The common implementation of the nonlinear optical (NLO) microscope uses a tight focal spot that is raster-scanned rapidly across the sample. The light source is chosen such that the pulse conditions in focus are optimal for generating the highest amount of signal in the shortest amount of time without altering the sample. Nonlinear optical processes are more efficient for higher peak powers, which can be achieved by shortening the pulses while keeping the average power below the limits set by linear heating of the sample. At the same time, the sampling rate is improved by increasing the pulse repetition rate. For this reason, femtosecond laser oscillators with repetition rates in the 50–100 MHz range have become the standard light source in NLO microscopy, in particular for use in two-photon excited fluorescence (TPEF) and SHG imaging studies [51], [52].

For vibrational microscopy, spectral resolution is an additional requirement. The use of picosecond light sources constitutes a straightforward solution. Although picosecond pulse trains offer lower peak powers compared to femtosecond pulse trains at the same average power, they provide pulses with spectral widths that comply with the linewidths of the vibrational spectrum ($\sim 10\text{cm}^{-1}$), enabling selective excitation of vibrational modes. Picosecond lasers, often in combination with a synchronously pumped optical parametric oscillator (OPO), have successfully powered CRS microscopes for the last 15 years or so [53], [54], [61]. These sources provide pump and Stokes beams with average powers and pulse energies in the range of 5–30 mW and 60–320 pJ at the sample, respectively, which produce strong CRS signals at $\sim 1 \mu$s pixel dwell times in a typical laser scanning microscope.

The OPOs used in CRS microscopy produce signal (ω_s) and idler (ω_i) beams. Whereas the ω_s beam is often used in combination with the pump laser beam (ω_p) for NIR illumination of the sample in CRS imaging, the idler beam extends out to much longer wavelengths. OPOs pumped by the fundamental of ps Nd:vanadate or Yb-fiber lasers deliver idler beams that are tunable into part of the MIR (2.2–4.8 μm), corresponding to the vibrational energies of C-H, O-H and N-H stretching modes. Consequently, such light sources are not only suitable for CRS, but also for SFG [24], [28] and TSFG vibrational imaging.

For the triple-modal vibrational imaging studies described here, we use a 10 W Yb-fiber laser (aeroPULSE, NKT Photonics) that produces 5 ps pulses with a center wavelength of 1030 nm and a pulse repetition rate of 76 MHz. The 1030 nm beam pumps a synchronously pumped OPO (Levante IR ps, APE Berlin), which delivers a signal (1.35–2.00 μm) and idler (2.2–4.7 μm) beam. The combination of the fundamental, signal and idler enable CARS, SFG and TSFG with a single light source. For CARS, we use the fundamental as the ω_p beam and the signal as the Stokes ω_S beam. To drive the 2845 cm^{-1} vibrational mode, the Stokes is tuned to 1460 nm with the pump fixed at 1030 nm, producing an anti-Stokes signal at 796 nm. For SFG, we use the idler as the ω_{IR} beam and the fundamental as the ω_p
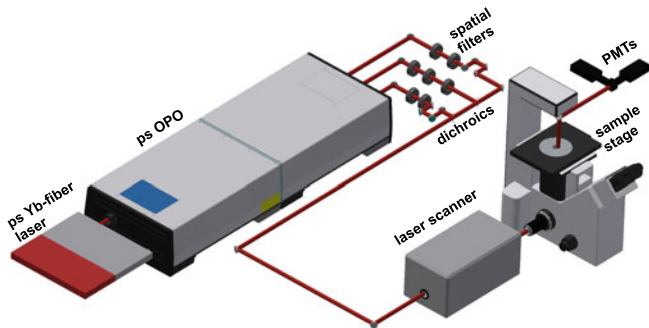
Fig. 2. Schematic of the triple-modal vibrational microscope system. The synchronously-pumped OPO delivers three beams (ω_p, ω_S and ω_{IR}) that are properly conditioned, delayed and collinearly combined on dichroic mirrors. The imaging platform is a modified laser-scanning microscope, optimized for NIR and MIR throughput. The condenser lens and detection bandpass filters are not explicitly shown in this schematic.

Fig. 3. Lateral pointspread function measurements with BaTiO$_3$ nanoparticles. (a) SHG and CARS, (b) SFG and TSFG.

beam. The vibrational energy of 2845 cm^{-1} corresponds to an idler wavelength of 3515 nm, generating a SFG signal at 796 nm (same as in CARS). The same combination of beams is used for TSFG imaging, using the ω_p beam twice for the up-conversion. For the 2845 cm^{-1} mode, the TSFG signal appears at 449 nm. Tuning of the vibrational resonances in SFG and TSFG is accomplished by spectrally tuning the idler (ω_{IR}) beam. With the pump beam fixed at 1030 nm, the signal wavelength thus varies when probing different vibrational energies.

Before sending the excitation beams into the laser-scanning microscope, they are each conditioned with spatial filters, properly delayed with translation stages and collinearly combined at custom dichroic mirrors (Layertec, GmbH). A schematic of the setup is shown in Fig. 2.

B. Microscope

Because commercial laser-scanning microscopes are optimized for visible to NIR light, the incorporation of an additional MIR excitation beam requires a few modifications of the imaging system. Our imaging platform is based on an Olympus Fluoview 300 scan system interfaced with an Olympus IX71 microscope frame. The galvanometric mirrors are aluminum coated, which provides sufficient reflectivity in the 1.0–4.5 μm range. The scan lens is replaced with a CaF$_2$ lens of similar focal length. Calcium fluoride exhibits excellent transmissive properties in both the NIR and MIR range. Similarly, the tube lens in the IX71 from is replaced by a 180 mm CaF$_2$ lens. We use a 74x, 0.65 NA reflective objective (5007, Beck), which is a Cassegrain design with a central obscuration. Typical average powers at the sample are 10–40 mW for the ω_p and ω_S beams and 1-5 mW for the ω_{IR} beam.

Because all of the signals in the triple-modal vibrational microscope are in the visible/NIR range, standard refractive optics can be used to relay the radiation to the detection channels. The signal is collected in the forward propagating direction with an achromatic/aplanatic condenser lens with oil immersion (Olympus), which features an adjustable detection numerical aperture (max. NA = 1.40). The signal is split with a dichroic mirror into two detection channels, each equipped with switchable bandpass
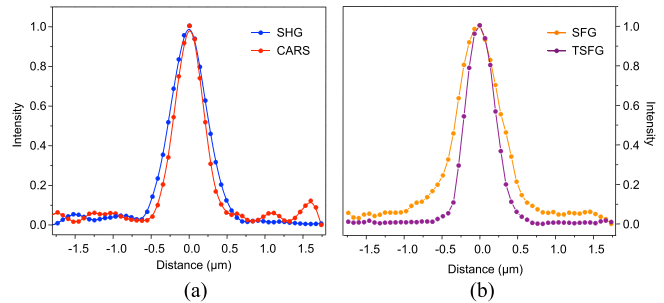
filters (Semrock). It is also possible to capture the signal in the epi-direction [24], however, for the experiments reported in this contribution all signals are collected in the forward direction.

C. Signal Detection

We employ two photomultiplier tube (PMT) detection channels. One channel uses a Hamamatsu 7422-40 (blue-sensitive) detector, and the other channel uses a 7422-50 (red-sensitive) detector. Both PMTs are equipped with a Thorlabs TIA60 preamplifier. A single photon counting scheme is used to reduce background noise. For this purpose, the electron bursts are passed through a discriminator (F-100T, Advanced Research Instruments), which converts detection events into TTL pulses. The TTL pulses are conditioned with a waveform generator (AFG3102, Tektronix) for optimum registration and integration by the Fluoview acquisition card.

The red-sensitive PMT is used for detecting SFG or CARS, while the blue sensitive PMT is utilized for detecting the SHG or TSFG signals. Note that the SFG and CARS signals arrive at the same wavelength and cannot be discriminated with bandpass filters. Therefore, the SFG and CARS signals are detected consecutively. SFG images are obtained when the ω_s beam is blocked, while CARS images are acquired when the ω_i beam is blocked.

IV. IMAGING PROPERTIES

A. Spatial Resolution

One of the defining features of the nonlinear vibrational microscope is its ability to visualize structures at high spatial resolution. The spatial resolution is primarily determined by the properties of the microscope objective lens. The Schwarzschild-type Cassegrain objective used here has a nominal NA of 0.65, allowing sub-μm lateral resolution while offering a relatively low axial resolution ($> 10~\mu$m) [55], [56]. We have characterized the lateral resolution with 0.3 μm barium titanate (BaTiO$_3$) nanoparticles for the different modalities supported by the imaging platform. BaTiO$_3$ particles are used because they exhibit a strong and nonvanishing $\chi^{(2)}$, while also featuring a $\chi^{(3)}$ of sufficient magnitude to visualize single particles.

Fig. 3(a) shows the SHG (blue) and CARS (red) signal obtained when scanning the focal spot across an individual particle. The FWHM of the profile is 0.55 μm for SHG and 0.44 μm for
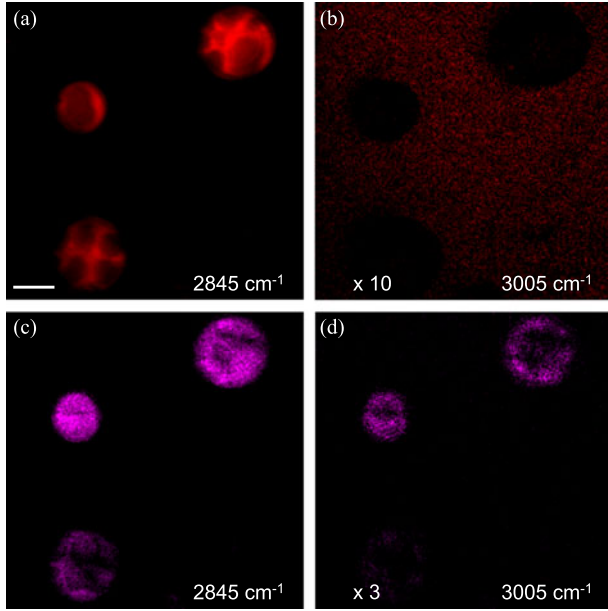
Fig. 4. Vibrational imaging of immersion oil droplets in D_2O. (a) CARS at 2845 cm^{-1}, (b) CARS at 3005 cm^{-1} multiplied by 10 times relative to the signal at 2845 cm^{-1}, (c) TSFG at 2845 cm^{-1}, (d) TSFG at 3005 cm^{-1} multiplied by 3 times relative to the signal at 2845 cm^{-1}. Scale bar is 10 μm.
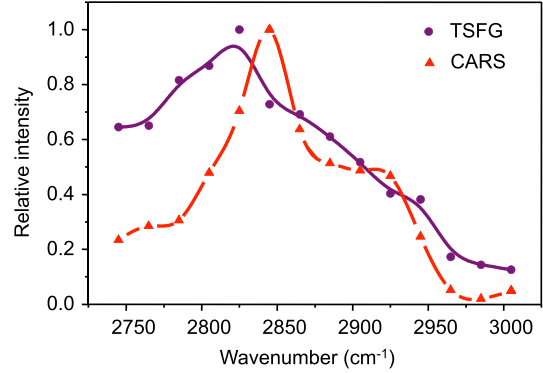

Fig. 5. Spectral dependence of the CARS (red triangles) and TSFG (purple dots) signal obtained from the immersion oil droplets shown in Fig. 4. Solid lines are a guide for the eye.

CARS, which is a representative measure for the resolution attainable in the microscope. The tighter focal spot for CARS is expected because of the higher nonlinearity of the process. The corresponding SFG and TSFG profiles are depicted in Fig. 3(b). We find a FWHM of 0.66 μm for SFG and 0.45 μm for TSFG. Note that even though the vibrational resonance is driven with light in the MIR, here for wavelengths in the 3–4 μm range, the lateral resolution in both SFG and TSFG is well below a μm. Compared to FTIR microscopy techniques, the up-conversion step in SFG and TSFG permits IR-based vibrational imaging at essentially sub-diffraction limited resolution.

B. Spectral Dependence

The spectral dependence of the CARS and SFG techniques has been discussed extensively in the literature [2], [17], [33], [41]. Therefore, we will focus mainly on the spectral dependence of the TSFG signal, which has not been reported before. In Fig. 4, we compare the CARS image of droplets of immersion oil in D_2O with the corresponding TSFG image. When the $\omega_p - \omega_S$ frequency is tuned to 2845 cm^{-1}, the symmetric stretching mode of the methylene group, the droplets are clearly visible in the CARS image displayed in Fig. 4(a). While the resonant contribution of the methylene mode is strong, the nonresonant background signal from D_2O is very weak, producing an image with high contrast. Tuning to 3005 cm^{-1}, off-resonance with the methylene mode, produces much a lower signal and an image with characteristically inverted contrast due to destructive interference with the nonresonant background. The internal structure of the oil in panel (a) can possibly be ascribed to interferences between the two coverslips between which the droplets are sandwiched. Nonetheless, this accidental image

feature helps to point out differences between the CARS and the TSFG channel, which is why we choose to display it here.

The corresponding TSFG image taken at 2845 cm^{-1} is shown in Fig. 4(c). Although weaker as in CARS, the signal from the droplets is well above the background signal from D_2O. When tuning to the 3005 cm^{-1} vibrational energy, the signal is substantially weaker, although the signal of the oil droplets remains above the background signal. These images show that TSFG, like CARS, enables vibrational imaging of isotropic materials like liquid oil. Whereas CARS visualizes the oil through a Raman process, TSFG probes the material through a dipole-allowed transition. In both cases, the image contrast arises because of the selective driving of the methylene vibrational mode.

The spectral dependence of the CARS and TSFG signals from the immersion oil is shown in Fig. 5. The CARS signal shows a band profile that is characteristic for CARS spectra of aliphatic molecules. The peak at 2845 cm^{-1} is attributed to the aforementioned methylene symmetric stretching mode. The signal dips near 2980 cm^{-1}, which is to interference with the nonresonant background. The TSFG spectrum also shows a maximum and a minimum in this range, but the overall shape is different. First, the offset of the signal at lower energies, due to the nonresonant background, is significantly higher compared to CARS. Second, due to a higher contribution of the nonresonant signal, the bandshape is more dispersive. The maximum of the TSFG signal, also assigned to the methylene symmetric stretch, is red-shifted relative to the CARS spectrum. These observations indicate that for the oil sample studied here, the $\chi_r^{(3)}/\chi_{nr}^{(3)}$ ratio for TSFG is lower than for CARS. Note that the dispersive lineshape is a direct consequence of the coherent character of the TSFG signal.

It is interesting to compare the TSFG signal from aliphatic compounds with the THG signal from lipid droplets. In THG imaging it is known that the $\chi_{nr}^{(3)}(-3\omega; \omega, \omega, \omega)$ of lipids is significantly higher than the $\chi_{nr}^{(3)}$ of the surrounding aqueous medium [57]. The difference in the nonresonant response makes it possible to visualize lipid droplets in THG. In TSFG, we also find a relatively high $\chi_{nr}^{(3)}(-2\omega_p - \omega_{IR}; \omega_{IR}, \omega_p, \omega_p)$ from the aliphatic material versus the aqueous medium. In addition, TSFG exhibits a vibrationally resonant contribution, which
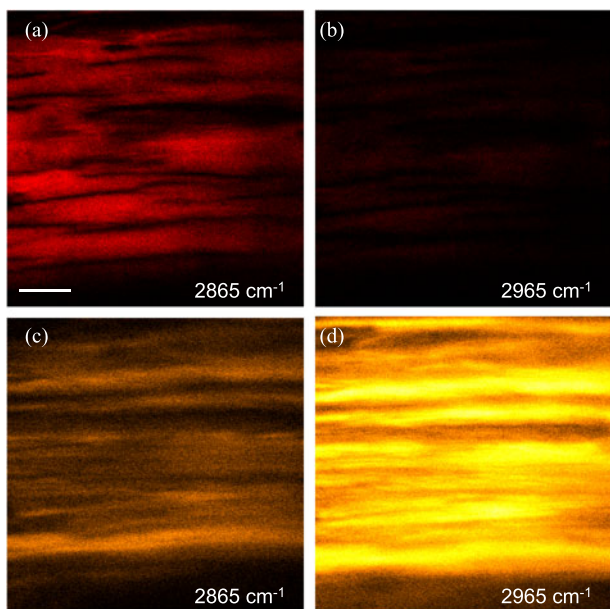
Fig. 6. Vibrational imaging of rat tail tendon. (a) CARS at 2865 cm^{-1}, (b) CARS at 2965 cm^{-1}, (c) SFG at 2865 cm^{-1}, (d) SFG at 2965 cm^{-1}. Scale bar is 10 μm.
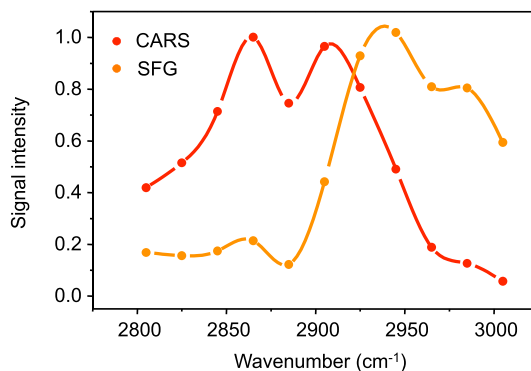

Fig. 7. Spectral dependence of the CARS (red dots) and SFG (orange dots) signal obtained from the rat tail tendon images shown in Fig. 6. Solid lines are a guide for the eye.

is absent in nonresonant THG. The $\chi_r^{(3)}$ contribution is sufficient to generate images with clear vibrational contrast, as is evident from Fig. 4.

Fig. 6 compares the CARS and SFG images of rat tail tendon. This tissue is rich in aligned collagen I fibers. The noncentrosymmetry of the collagen I fibrils gives rise to a strong SFG signal. Panels 6(a) and (c) show the CARS and SFG images, respectively, when tuning to a vibrational energy of 2865 cm^{-1}. Note that the spatial features of the fibrous tissue appear differently in these modalities. Whereas CARS is sensitive to the bulk architecture of the tissue, the SFG images shows more refined fibrous details. Similar to SHG imaging, SFG is sensitive to the polar alignment of fiber domains, introducing $\chi^{(2)}$-specific image features related to average polar alignment of the collagen moieties [30], [58]. The latter features are not observed in the CARS image.

Panels 6(b) and (d) show the corresponding CARS and SFG images when tuning to 2965 cm^{-1}. While the CARS signal has diminished at this vibrational energy, the SFG signal has increased. Collagen I is rich in methylene groups and has a relatively low density of methyl groups, underlining that the vibrational spectrum in the CH-stretching range is dominated mostly by methylene modes. Yet, the CARS and SFG spectral response of the sample is markedly different. The differences are exemplified in Fig. 7, which shows the CARS and SFG spectra extracted from a hyperspectral data stack. The CARS spectrum shows two maxima in this range, previously attributed to the symmetric and asymmetric CH$_2$ stretching modes [59]. The SFG spectrum exhibits a remarkably different profile, with a maximum near 2950 cm^{-1}. Although the origin of this peak is not entirely clear, it has been proposed before that a Fermi-resonance between the CH$_2$ stretching and bending overtone might be responsible for this signature [60]. The comparison

between the CARS and SFG spectrum thus reveals that the two different modalities illuminate very different spectroscopic details of the sample, providing complementary information about content and structure.

C. Image Features

The Cassegrain objective lens exhibits a central obscuration, resulting in annular illumination with an extended focal range. The focal distribution shares similarities with a Bessel beam, which also features an extended axial focal profile. Despite these focal properties, the nonlinear optical processes discussed here all produce detectable signals, captured by the high NA condenser lens. The CARS signal yields contrast similar to what is observed under tight focusing with a high NA refractive objective [61], indicating that the phase-matching conditions for CARS are not significantly altered by the use of the reflective lens. Previous work has also shown that SHG from non-centrosymmetric materials such as collagen fibers, obtained with a reflective objective, appear with image features that are comparable to SHG signals generated by refractive objectives [62]. Similarly, the detectable SFG and TSFG signals from bulk materials suggest that the coherent radiation appears at phase-matching angles that are within the cone angle of the 1.4 NA condenser lens.

As shown in Fig. 4, TSFG is obtained from the bulk oil medium. No particular highlighting of D$_2$O/oil interfaces is observed. These imaging properties are notably different from what is commonly seen in THG microscopy with high NA refractive lenses, where bulk signals are not allowed because of the Gouy phase-mismatch. The detected TSFG response from the bulk suggests that a similar Gouy phase-mismatch is not suppressing the signal in the detection direction. As discussed in Section II-D, the Gouy phase mismatch in vibrationally-sensitive TSFG is relaxed relative to THG because of the longer wavelength of one of the light-matter interactions. Also, in the case of perfect Bessel beams, it is known that phase matching for THG can be achieved at an off-axis angle in bulk materials [50], [63]. This latter mechanism may partially contribute to the detectable bulk signals encountered in the current TSFG imaging experiments.
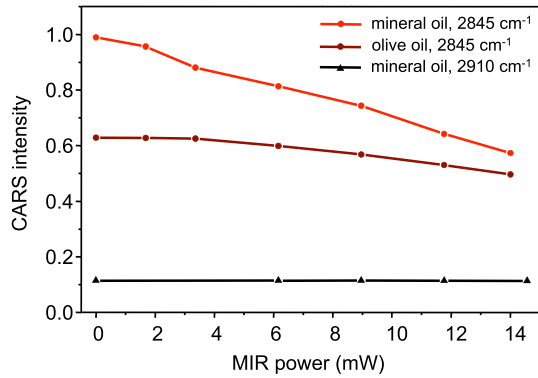
Fig. 8. CARS intensity as a function of average power of focused MIR radiation. Average power is measured at the sample location.

Fig. 9. Multi-modal vibrational imaging of a cellulose granule. (a) CARS at 2845 cm^{-1}, (b) SHG, (c) TSFG at 2845 cm^{-1}, and (d) SFG at 2845 cm^{-1}. Scale bar is 10 μm.

Compared to the CARS and SFG signals, the TSFG signal is about 5 times weaker under resonant conditions. Yet, the TSFG signal clearly stands out against other spurious signals. We do not observe a strong multi-photon fluorescence signal in the TSFG channel, as the signal disappears when the detection bandpass spectral window is red-shifted by 50 nm to exclude the 449 nm TSFG signal wavelength. Since fluorescence emission is typically broadband, a substantial portion of the signal would be expected at the detector upon red-shifting the detection window, if the origin of the signal were fluorescence. The signal in the TSFG channel also disappears if either one of the ω_p and ω_{IR} beams is blocked or when the two pulse trains are temporally offset beyond the width of the pulses (5 ps).

V. IR-Induced Effects on CARS

The addition of a MIR beam to the NLO laser-scanning microscope not only enables the implementation of the vibrationally-sensitive SFG and TSFG modules, but also offers an opportunity to study other MIR-induced effects. One such effect is shown in Fig. 8, where the CARS signal from immersion oil is studied while the sample is illuminated by the additional MIR-beam. We observe that the on-resonance CARS signal decreases for higher average power of the MIR-beam, both for the immersion oil and a sample of olive oil. When the MIR beam is tuned to 2910 cm^{-1}, away from the dominant symmetric methylene vibration, the depletion of the CARS signal is significantly less.

These observations indicate that a vibrational-selective excitation by the MIR beam alters the magnitude of the CARS signal. A possible explanation is the change in the refractive properties of the material after vibrational heating of the sample, which changes the focusing properties in the medium and can thus affect the amount of signal intercepted by the condenser lens. Such a process is reminiscent of the mechanism behind photothermal MIR imaging, which uses the refractive changes experienced by a vis/NIR probe beam due to the MIR excitation of the material [64], [65]. In the present case, the heating induced by the MIR excitation would defocus the anti-Stokes radiation and reduce the amount of signal captured by the collimating lens. However, we find that changing the NA of the condenser in the 0.7–1.4 NA range does not dramatically alter the depletion trend shown in Fig. 8.
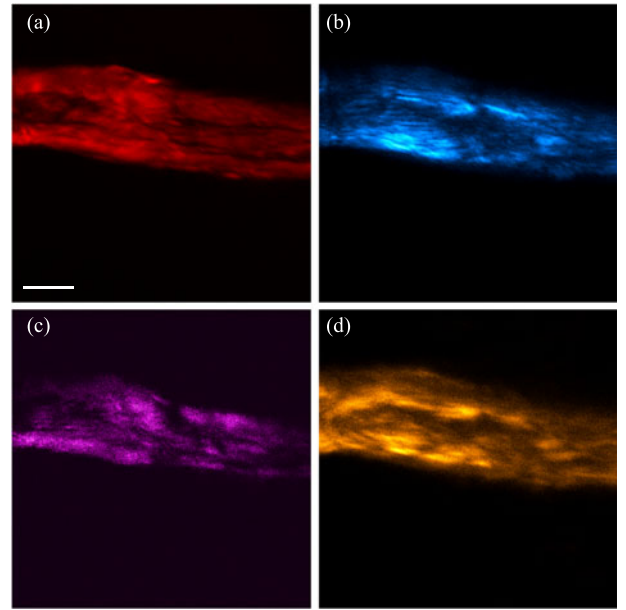
Ground state depletion is an alternative mechanism that could lead to a decrease of the CARS signal. By transferring population from the ground state to the vibrationally excited state, the ground state population becomes depleted and the regular parametric CARS pathway is blocked. The latter process can be useful in potential super-resolution techniques [66], [67]. In either case, the IR-beam offers a mechanism for controlling the amount of detected CARS signal, which could have interesting future applications.

VI. Triple-Modal Vibrational Imaging

The examples shown in Figs. 4 and 6 highlight some of the capabilities of the triple-modal vibrational microscope. Another example is given in Fig. 9 where a cellulose granule is visualized with CARS, SFG, TSFG and SHG. Since cellulose has a non-vanishing $\chi^{(2)}$, it is suitable for detailed investigations using all four imaging modalities. Cellulose has been studied rather extensively with CARS and SHG microscopy [68]–[70], but the example shown here underlines that high resolution images can be obtained with the SFG and TSFG modalities as well. This capability is useful for an in-depth analysis of microdomains, which is relevant for understanding the spatial heterogeneity of cellulose hydrolysis kinetics [70]. In particular, SFG spectroscopic contrast provides a wealth of information about chain orientation and packing density [71]–[73].

VII. Prospects and Challenges

In this contribution, we discussed an imaging platform that integrates three vibrationally sensitive imaging modalities, namely CARS, SFG and TSFG. Whereas CARS probes Raman-active modes, TSFG is sensitive to IR-active modes. In addition, the SFG modality enables spectroscopic studies of

non-centrosymmetric materials. The combination of these three modalities allows for a complete vibrational spectroscopic assessment of the sample. All imaging techniques offer sub-μm lateral resolution, which, for the IR-based modalities, represents an effective sub-diffraction limited resolution compared to IR-absorption microscopy.

Among the available coherent vibrational techniques, the TSFG modality has not been previously demonstrated. The images presented in this work underline that TSFG signals are at detectable levels that are suitable for laser scanning microscopy applications, at least for organic materials examined in the CH-stretching range of the spectrum. We have shown that the TSFG signal is vibrationally sensitive, but that the $\chi_r^{(3)}/\chi_{nr}^{(3)}$ ratio is lower than for CARS. In this context it is relevant to emphasize that the resonant response of the IR-active CH stretching modes is much weaker than the response of various modes in the fingerprint region (1000–1800 cm^{-1}). For instance, the Amide I mode exhibits an absorption cross section that is about an order of magnitude higher than the corresponding response of the CH-stretching modes, implying that $\chi_r^{(3)}$ for the Amide I mode is significantly higher. Since TSFG scales as $|\chi_r^{(3)}|^2$, the TSFG signals in the fingerprint range are expected to be substantial. In addition, the dispersive character of TSFG in this range is expected to be reduced. Therefore, TSFG imaging may be particularly useful for mapping modes in the fingerprint range. Although our current lightsource is not suitable for generating ω_{IR} in this region, future efforts will focus on pushing TSFG microscopy to the 1000–1800 cm^{-1} vibrational range.

One of the merits of TSFG is that it offers a nonlinear alternative to conventional IR microscopy. Although it is sensitive to the same vibrational modes as probed in FTIR microscopy, the signal is detected in the visible range of the spectrum, thus greatly simplifying the detection strategy. In addition, the lateral resolution is beyond the IR-diffraction limit, allowing the generation of images with IR contrast with $\sim 0.5~\mu$m resolution. This resolution is predominantly determined by the two-photon upconversion process rather than by the ω_{IR} interaction. Consequently, the high resolution can be maintained independent of the λ_{IR} wavelength. In this regard, the TSFG shares similarities with photothermal IR imaging techniques. [64], [65] A potential advantage of TSFG imaging over photothermal approaches is that no modulation scheme is required and that the spatial resolution is not directly linked to heat diffusion. Because TSFG relies on optically driven vibrational coherences, it is not directly sensitive to photothermal populations, implying that the imaging resolution is expected to be independent of material or position in the sample.

The combination of different vibrational NLO techniques on a single platform is helpful for a deeper spectroscopic assessments of samples. For instance, it can be challenging to analyze biomolecular microcrystals in complex media when the exact chemical composition is unknown. Since many biomolecules form non-centrosymmetric crystals, they can be assessed by SFG in addition to CARS and TSFG microscopy. The ability to selectively sample IR and Raman-active modes, as offered through TSFG and CARS, respectively, can help determine the spectroscopic mode symmetries and thus information

about chemical content and molecular orientation. The SFG information, aided by polarization-sensitive measurements, can furthermore provide information about structure and orientation that complement the bulk-sensitive TSFG and CARS measurements. Potential examples include the study of microcrystallites in atherosclerotic lesions [74], microdomains in cellulose [68]–[70], and nucleation of polypeptide crystals [75].

However, the triple-modal vibrational microscope is not without its limitations. Because it combines NIR with MIR incident beams, optical elements are needed that are non-standard on regular laser-scanning microscopes. The large spectral gap between the NIR and MIR excitation beams implies that optical components need to be chosen that operate over a broad wavelength range. This requirement holds not only for sample substrates, but also for lenses and relay optics. Although all-reflective imaging systems represent a broadband and achromatic solution [62], [65], such optical components are not easily integrated into conventional laser scanning microscopes. Broadband refractive components, such as the CaF$_2$ lenses used here, retain the original design of the laser-scanning microscope while expanding its transmission range into the MIR. Nonetheless, singlet optical elements such as CaF$_2$ lenses introduce chromatic aberrations, which ultimately limit the image quality. In this regard, the development of achromatic broadband lenses would significantly impact the practical implementation of the NLO multimodal vibrational microscope.

Another limitation is the elongated focal volume associated with the use of a Cassegrain reflective lens. The extended axial focal range deteriorates the axial resolution and reduces the sensitivity of the microscope to sub-μm structures. Alternative reflective lens designs, which produce focal volumes that exhibit a higher degree of 3D confinement, would be welcome. Although the design criteria are rather challenging, refractive objective lenses capable of achromatically focusing light in the 1–4.5 μm range to a tight spot are also desirable. Developments in this area are sure to improve the utility of the triple-modal vibrational microscope.

VIII. Conclusion

In this contribution, we introduced the principle of triple-modal vibrational imaging with contrast generated by CARS, SFG and TSFG. The spectral properties of these modalities complement each other, enabling a more complete spectroscopic assessment of the sample at the sub-μm scale. The implementation discussed in this work emphasizes the feasibility of multimodal vibrational contrast, including the practicality of TSFG microscopy, a new technique that provides images based on the excitation of IR-active vibrational modes. We expect that with further improvements of broadband optical elements, the use of IR-based vibrational technologies will grow in importance in laser-scanning NLO microscopy of biological materials.

References

[1] S. Mukamel, *Principles of Nonlinear Optical Spectroscopy*. New York, NY, USA: Oxford Univ. Press, 1995.

[2] J. X. Cheng and X. S. Xie, *Coherent Raman Scattering Microscopy*. Boca Raton, FL, USA: CRC Press, 2013.

[3] C. H. Camp and M. Cicerone, "Chemically sensitive bioimaging with coherent Raman scattering," *Nat. Photon.*, vol. 9, pp. 295–305, Apr. 2015.

[4] R. C. Prince, R. Frontiera, and E. O. Potma, "Stimulated Raman scattering: From bulk to nano," *Chem. Rev.*, vol. 117, no. 7, pp. 5070–5094, Apr. 2017.

[5] C. L. Evans *et al.*, "Chemical imaging of tissue in vivo with video-rate coherent anti-Stokes Raman scattering microscopy," *Proc. Nat. Acad. Sci*, vol. 102, no. 46, pp. 16807–16812, Nov. 2005.

[6] B. G. Saar *et al.*, "Video-rate molecular imaging in vivo with stimulated Raman scattering," *Science*, vol. 330, no. 6009, pp. 1368–1370, Dec. 2010.

[7] T. T. Le, S. Yue, and J.-X. Cheng, "Shedding new light on lipid biology with coherent anti-Stokes Raman scattering microscopy," *J. Lipid Res.*, vol. 51, pp. 3091–3102, Aug. 2010.

[8] H. J. Lee and J.-X. Cheng, "Imaging chemistry inside living cells by stimulated Raman scattering microscopy," *Methods*, vol. 128, pp. 119–128, Jul. 2017.

[9] M. Windbergs *et al.*, "Chemical imaging of oral solid dosage forms and changes upon dissolution using coherent anti-stokes Raman scattering microscopy," *Anal. Chem.*, vol. 81, no. 6, pp. 2085–2091, Feb. 2009.

[10] M. N. Slipchenko *et al.*, "Vibrational imaging of tablets by EPI-detected stimulated Raman scattering microscopy," *Analyst*, vol. 135, no. 10, pp. 2613–2619, Oct. 2010.

[11] C. J. Strachan, M. Windbergs, and H. L. Offerhaus, "Pharmaceutical applications of non-linear imaging," *Int. J. Pharm.*, vol. 417, no. 1–2, pp. 163–172, Sep. 2011.

[12] T. Meyer *et al.*, "Three-dimensional molecular mapping of a multiple emulsion by means of CARS microscopy," *J. Phys. Chem. B*, vol. 112, no. 5, pp. 1420–1426, Jan. 2008.

[13] M. B. J. Roeffaers *et al.*, "Label-free imaging of biomolecules in food products using stimulated Raman microscopy," *J. Biomed. Opt.*, vol. 16, no. 2, Feb. 2011, Art. no. 021118.

[14] B. von Vacano, L. Meyer, and M. Motzkus, "Rapid polymer blend imaging with quantitative broadband multiplex CARS microscopy," *J. Raman Spectrosc.*, vol. 38, no. 7, pp. 916–926, Apr. 2007.

[15] Y. J. Lee, D. Moon, K. B. Migler, and M. T. Cicerone, "Quantitative image analysis of broadband CARS hyperspectral images of polymer blends," *Anal. Chem.*, vol. 83, no. 7, pp. 2733–2739, Mar. 2011.

[16] R. C. Burruss, A. D. Slepkov, A. F. Pegoraro and A. Stolow, "Unraveling the complexity of deep gas accumulations with three-dimensional multimodal CARS microscopy," *Geology*, vol. 40, no. 12, pp. 1063–1066, Dec. 2012.

[17] Y. R. Shen, "Surface properties probed by second-harmonic and sum-frequency generation," *Nature*, vol. 337, pp. 519–525, Feb. 1989.

[18] K. B. Eisenthal, "Liquid interfaces probed by second-harmonic and sum-frequency spectroscopy," *Chem. Rev.*, vol. 96, no. 4, pp. 1343–1360, Jun. 1996.

[19] M. Flörsheimer, C. Briller, and H. Fuchs, "Chemical imaging of interfaces by sum-frequency microscopy," *Langmuir*, vol. 15, pp. 5437–5439, 1999.

[20] D. M. P. Hoffmann, K. Kuhnke, and K. Kern, "Sum-frequency generation microscope for opaque and reflecting samples," *Rev. Sci. Instrum.*, vol. 73, pp. 3221–3226, 2002.

[21] K. A. Cimatu and S. Baldelli, "Chemical microscopy of surfaces by sum frequency generation imaging," *J. Phys. Chem. C.*, vol. 113, pp. 16575–16588, 2009.

[22] K. Locharoenrat, H. Sano, and G. Mizutani, "Demonstration of confocal sum frequency microscopy," *Phys. Status Solidi C.*, vol. 6, pp. 304–306, 2009.

[23] K. Inoue, M. Fujii, and M. Sakai, "Development of a non-scanning vibrational sum-frequency generation detected infrared super-resolution microscope and its application to biological cell," *Appl. Spectrosc.*, vol. 64, pp. 275–281, 2010.

[24] V. Raghunathan, Y. Han, O. Korth, N. H. Ge, and E. O. Potma, "Rapid vibrational imaging with sum frequency generation microscopy," *Opt. Lett.*, vol. 36, pp. 3891–3893, 2011.

[25] K. A. Smith and J. C. Conboy, "A simplified sum-frequency vibrational imaging setup used for imaging lipid bilayer arrays," *Anal. Chem.* vol. 84, pp. 8122–8126, 2012.

[26] C. M. Lee, K. Kafle, S. Huang, and S. H. Kim, "Multimodal broadband vibrational sum frequency generation (MM-BB-V-SFG) spectrometer and microscope," *J. Phys. Chem. B.*, vol. 120, pp. 102–116, 2016.

[27] H. Wang, T. Gao, and W. Xiong, "Self phase-stabilized heterodyne vibrational sum frequency generation microscopy," *ACS Photon.*, vol. 4, pp. 1839–1845, 2017.

[28] A. M. Hanninen, M. W. Shu, and E. O. Potma, "Hyperspectral imaging with laser-scanning sum-frequency generation microscopy," *Biomed. Opt. Express*, vol. 8, no. 9, pp. 4230–4242, Sep. 2017.

[29] F. S. Pavone and P. J. Campagnola, *Second Harmonic Generation Imaging*. Boca Raton, FL, USA: CRC Press, 2013.

[30] Y. Han *et al.*, "Mapping molecular orientation with phase sensitive vibrationally resonant sum-frequency generation microscopy," *J. Phys. Chem. B*, vol. 117, pp. 6149–6156, 2013.

[31] Y. Han, J. Hsu, N. H. Ge, and E. O. Potma, "Polarization-sensitive sum-frequency generation microscopy of collagen fibers," *J. Phys. Chem. B*, vol. 119, pp. 3356–3365, 2015.

[32] H. C. Hieu, N. A. Tuan, H. Li, Y. Miyauchi, and G. Mizutani, "Sum frequency generation microscopy study of cellulose fibers," *Appl. Spectrosc.* vol. 65, pp. 1254–1259, 2011.

[33] C. Y. Chung, J. Boik, and E. O. Potma, "Biomolecular imaging with coherent nonlinear vibrational microscopy," *Annu. Rev. Phys. Chem.*, vol. 64, pp. 77–99, Apr. 2013.

[34] H. Segawa *et al.*, "Label-free tetra-modal molecular imaging of living cells with CARS, SHG, THG and TSFG (coherent anti-Stokes Raman scattering, second harmonic generation, third harmonic generation and third-order sum frequency generation)," *Opt. Express*, vol. 20, no. 9, pp. 9551–9557, Apr. 2012.

[35] H. Segawa *et al.*, "Electronically resonant third-order sum frequency generation spectroscopy using a nanosecond white-light supercontinuum," *Opt. Express*, vol. 22, no. 9, pp. 10416–10429, Apr. 2014.

[36] Y. Barad, H. Eisenberg, M. Horowitz, and Y. Silberberg, "Nonlinear scanning laser microscopy by third harmonic generation," *Appl. Phys. Lett.*, vol. 70, no. 8, pp. 922–924, Feb. 1997.

[37] J. A. Squier, M. Müller, G. J. Brakenhoff, and K. R. Wilson, "Third harmonic generation microscopy," *Opt. Express*, vol. 3, no. 9, pp. 315–324, Oct. 1998.

[38] D. Yelin and Y. Silberberg, "Laser scanning third-harmonic-generation microscopy in biology," *Opt. Express*, vol. 5, no. 8, pp. 169–175, Oct. 1999.

[39] M. Bonn *et al.*, "Novel surface vibrational spectroscopy: Infrared-infrared-visible sum-frequency generation," *Phys. Rev. Lett.*, vol. 86, no. 8, pp. 1566–1569, Feb. 2001.

[40] A. J. Traverso *et al.*, "Two-photon infrared resonance can enhance coherent Raman scattering," *Phys. Rev. Lett.*, vol. 120, no. 6, Feb. 2018, Art. no. 063602.

[41] H.-F. Wang, W. Gan, R. Lu, Y. Rao, and B.-H. Wu, "Quantitative spectral and orientational analysis in surface sum frequency generation vibrational spectroscopy (SFG-VS), " *Int. Rev. Phys. Chem.*, vol. 24, no. 2, pp. 191–256, Apr.–Jun. 2005.

[42] V. N. Denisov, B. N. Mavrin, and V. B. Podobedov, "Hyper-Raman scattering by vibrational excitations in crystals, glasses and liquids," *Phys. Rep.*, vol. 151, no. 1, pp. 1–92, Jul. 1987.

[43] L. D. Ziegler, "Hyper-Raman spectroscopy," *J. Raman Spectrosc.*, vol. 21, no. 12, pp. 769–779, Dec. 1990.

[44] G. L. Eesley, *Coherent Raman Spectroscopy*. Oxford, U.K: Pergamon Press, 1981.

[45] S. Rahav and S. Mukamel, "Stimulated coherent anti-Stokes Raman spectroscopy (CARS) resonances originate from double-slit interference of two-photon Stokes pathways," *Proc. Nat. Acad. Sci*, vol. 107, no. 11, pp. 4825–4829, Mar. 2010.

[46] E. T. Garbacik *et al.*, "Background-free nonlinear microspectroscopy with vibrational molecular interferometry," *Phys. Rev. Lett.*, vol. 107, no. 25, Dec. 2011, Art. no. 253902.

[47] J.-X. Cheng, A. Volkmer, and X. S. Xie, "Theoretical and experimental characterization of coherent anti-Stokes Raman scattering microscopy," *J. Opt. Soc. Amer. B.*, vol. 19, no. 6, pp. 1363–1375, Jun. 2001.

[48] J.-X. Cheng and X. S. Xie, "Green's function formulation for third-harmonic generation microscopy," *J. Opt. Soc. Amer. B*, vol. 19, no. 7, pp. 1604–1610, Jul. 2002.

[49] L. Moreaux, O. Sandre, and J. Mertz, "Membrane imaging by second-harmonic generation microscopy," *J. Opt. Soc. Amer. B*, vol. 17, no. 10, pp. 1685–1694, Oct. 2000.

[50] D. Débarre, W. Supatto, and E. Beaurepaire, "Structure sensitivity in third-harmonic generation microscopy," *Opt. Lett.*, vol. 30, no. 16, pp. 2134–2136, Aug. 2005.

[51] J. A. Squier and M. Müller, "High resolution nonlinear microscopy: A review of sources and methods for achieving optimal imaging," *Rev. Sci. Instrum.*, vol. 72, no. 7, pp. 2855–2867, Jul. 2001.

[52] E. E. Hoover and J. A. Squier, "Advances in multiphoton microscopy technology," *Nat. Photon.*, vol. 7, pp. 93–101, Feb. 2013.

[53] J.-X. Cheng, A. Volkmer, L. D. Book, and X. S. Xie, "An epi-detected coherent anti-Stokes Raman scattering (E-CARS) microscope with high spectral resolution and high sensitivity," *J. Phys. Chem. B*, vol. 105, no. 7, pp. 1277–1280, Feb. 2001.

[54] F. Ganikhanov *et al.*, "Broadly tunable dual-wavelength light source for coherent anti-Stokes Raman scattering microscopy," *Opt. Lett.*, vol. 31, no. 9, pp. 1292–1294, May 2006.

[55] E. S. Lee, S. W. Lee, J. Hsu, and E. O. Potma, "Vibrationally resonant sum-frequency generation microscopy with a solid immersion lens," *Biomed. Opt. Express*, vol. 5, no. 7, pp. 2124–2134, Jun. 2014.

[56] N. Olivier, D. Débarre, P. Mahou, and E. Beaurepaire, "Third-harmonic generation microscopy with Bessel beams: a numerical study," *Opt. Express*, vol. 20, no. 22, pp. 24886–24902, Oct. 2012.

[57] D. Débarre *et al.*, "Imaging lipid bodies in cells and tissues using third-harmonic generation microscopy," *Nat. Methods*, vol. 3, no. 1, pp. 47–53, Jan. 2006.

[58] C. A. Couture *et al.*, "The impact of collagen fibril polarity on second harmonic generation microscopy," *Biophys. J.*, vol. 109, no. 12, pp. 2501–2510, Dec. 2015.

[59] H. W. Wang, T. T. Le, and J.-X. Cheng, "Label-free imaging of arterial cells and extracellular matrix using a multimodal CARS microscope," *Opt. Commun.*, vol. 281, no. 7, pp. 1813–1822, Apr. 2008.

[60] I. Rocha-Mendoza *et al.*, "Sum frequency vibrational spectroscopy: The molecular origins of the optical second-order nonlinearity of collagen," *Biophys. J.*, vol. 93, no. 12, pp. 4433–4444, Dec. 2007.

[61] S. Bégin *et al.*, "Coherent anti-Stokes Raman scattering hyperspectral tissue imaging with a wavelength-swept system," *Biomed. Opt. Express*, vol. 2, no. 5, pp. 1296–1306, Apr. 2011.

[62] B. Amirsolaimani, B., N. Peyghambarian, and K. Kieu, "All-reflective multiphoton microscope," *Opt. Express*, vol. 25, no. 19, pp. 23399–23407, Sep. 2017.

[63] S. P. Tewari, H. Huang, and R. W. Boyd, "Theory of third-harmonic generation using Bessel beams, and self-phase-matching," *Phys. Rev. A*, vol. 54, no. 3, pp. 2314–2325, Sep. 1996.

[64] E. S. Lee and J. Y. Lee, "High resolution cellular imaging with nonlinear optical infrared microscopy," *Opt. Express*, vol. 19, no. 2, pp. 1378–1384, Jan. 2011.

[65] D. Zhang *et al.*, "Depth-resolved mid-infrared photothermal imaging of living cells and organisms with submicrometer spatial resolution," *Sci. Adv.*, vol. 2, Sep. 2016, Art. no. e1600521.

[66] W. P. Beeker *et al.*, "A theoretical investigation of super-resolution CARS imaging via coherent and incoherent saturation of transitions," *J. Raman Spectrosc.*, vol. 42, no. 10, pp. 1854–1858, May 2011.

[67] C. Cleff *et al.*, "Ground-state depletion for subdiffraction-limited spatial resolution in coherent anti-Stokes Raman scattering microscopy," *Phys. Rev. A*, vol. 86, no. 2, Aug. 2012, Art. no. 023825.

[68] M. Zimmerley *et al.*, "Molecular orientation in dry and hydrated cellulose fibers: A coherent anti-Stokes Raman scattering microscopy study," *J. Phys. Chem. B*, vol. 114, no. 31, pp. 10200–10208, Jul. 2010.

[69] A. D. Slepkov, A. Ridsdale, A. F. Pegoraro, D. J. Moffatt, and A. Stolow, "Multimodal CARS microscopy of structured carbohydrate biopolymers," *Biomed. Opt. Express*, vol. 1, no. 5, pp. 1347–1357, Dec. 2010.

[70] A. Peciulyte, J. Kiskis, P. T. Larsson, L. Olsson, and A. Enejder, "Visualization of structural changes in cellulosic substrates during enzymatic hydrolysis using multimodal nonlinear microscopy," *Cellulose*, vol. 23, no. 3, pp. 1521–1536, Jun. 2016.

[71] C. M. Lee *et al.*, "Cellulose polymorphism study with sum-frequency-generation (SFG) vibration spectroscopy: Identification of exocyclic CH_2OH conformation and chain orientation," *Cellulose*, vol. 20, no. 3, pp. 991–1000, Jun. 2013.

[72] C. M. Lee *et al.*, "Hydrogen-bonding network and OH stretch vibration of cellulose: Comparison of computational modeling with polarized IR and SFG spectra," *J. Phys. Chem. B*, vol. 119, no. 49, pp. 15138–15149, Nov. 2015.

[73] C. M. Lee, X. Chen, P. A. Weiss, L Jensen, and S. H. Kim, "Quantum mechanical calculations of vibrational sum-frequency-generation (SFG) spectra of cellulose: dependence of the CH and OH peak intensity on the polarity of cellulose chains within the SFG coherence domain," *J. Phys. Chem. Lett.*, vol. 8, no. 1, pp. 55–60, Dec. 2016.

[74] J. L. Suhalim *et al.*, "Characterization of cholesterol crystals in atherosclerotic plaques using stimulated Raman scattering and second-harmonic generation microscopy," *Biophys. J.*, vol. 102, no. 8, pp. 1988–1995, Apr. 2012.

[75] L. M. Haupert and G. J. Simpson, "Screening of protein crystallization trials by second order nonlinear optical imaging of chiral crystals (SONICC)," *Methods*, vol. 55, no. 4, pp. 379–386, Dec. 2011.

Adam M. Hanninen received the B.S. degree in physics from the University of Minnesota, Minneapolis, MN, USA, in 2013 and is working toward the Ph.D. degree at the Department of Physics, University of California, Irvine, CA, USA. Under the direction of Prof. Potma, his research interests include the integration of the chemically selective sum-frequency generation modality into a multimodal microscope.

Richard C. Prince received the undergraduate degree from the University of Tennessee, Knoxville, TN, USA in 2015 with a B.A. in College Scholars Science Policy Emphases and Academic Physics and is working toward the Ph.D. degree at the Department of Biomedical Engineering, University of California, Irvine, CA, USA. His research interests include the development of hyperspectral vibrational microscopies and their application to a range of biological systems.

Eric O. Potma is a Professor with the Department of Chemistry at the University of California, Irvine (UCI), CA, USA. He holds adjunct positions with the Department of Electrical Engineering and Computer Science, and with the Beckman Laser Institute and Medical Clinic, UCI. His research group is active in developing nonlinear optical imaging techniques for the purpose of interrogating biological tissues, nanostructured materials, and individual molecules.